Control Engineering Practice 171 (2026) 106858

Contents lists available at ScienceDirect

Control Engineering Practice

journal homepage: www.elsevier.com/locate/conengprac

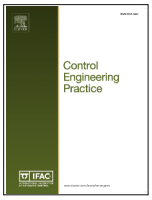

Actuator nonlinear dynamic inversion for the variable skew quad plane with heterogeneous motor dynamics

Tomaso De Ponti [a,*], Simon Hafner [b,a], Ewoud Smeur [a], Bart Remes [a]

[a] Faculty of Aerospace Engineering, Delft University of Technology, Kluyverweg 1, Delft, 2629 HS, Zuid-Holland, The Netherlands
[b] Institute of Flight System Dynamics, Technical University of Munich, Boltzmannstrasse 15, Garching near Munich, 85748, Bavaria, Germany

ARTICLE INFO

Keywords:
Actuator dynamics
Incremental nonlinear dynamic inversion (INDI)
Actuator nonlinear dynamic inversion (ANDI)
Heterogeneous actuators
Flight control
Vertical take-off and landing (VTOL)
Variable skew quad plane (VSQP)

ABSTRACT

Incremental Nonlinear Dynamic Inversion (INDI) has become a popular control strategy for unmanned aerial vehicles due to its disturbance rejection capabilities and minimal model reliance. However, its standard formulation neglects actuator dynamics, leading to undesired coupling in systems with heterogeneous actuator characteristics such as in the Variable Skew Quad Plane (VSQP). This paper analyzes the limitations of INDI in such scenarios and demonstrates how Actuator Nonlinear Dynamic Inversion (ANDI) solves them. The closed-loop transfer function analysis shows how ANDI eliminates cross-axis coupling by directly incorporating actuator dynamics into the control allocation process. Additionally, ANDI is compared to a modified INDI approach that employs lead-lag filters to homogenize actuator behavior. While this approach is effective in decoupling, it unnecessarily slows down system response and worsens saturation handling. Simulation and flight test results using the VSQP validate the theoretical findings, confirming that ANDI offers improved control accuracy on coupled axes without compromising performance on decoupled axes.

1. Introduction

Incremental Nonlinear Dynamic Inversion (INDI) control has become a widely popular control strategy in the field of Unmanned Aerial Vehicle (UAV) applications. It has been successfully implemented on a wide range of platforms, including multirotors (Smeur et al., 2018), fixed-wing aircraft (Pfeifle & Fichter, 2021), Vertical Take-Off and Landing (VTOL) vehicles (De Ponti et al., 2023), and even helicopters (Simplício et al., 2013).

One of the main advantages of INDI over, for example, traditional Proportional, Integral and Derivative (PID) control is its demonstrated capability for rapid disturbance rejection (Pfeifle & Fichter, 2021; Smeur et al., 2018, 2016b). Furthermore, unlike PID, INDI requires little or no gain scheduling. Additionally, INDI demands minimal model knowledge thanks to its sensor-based nature (Smeur et al., 2016a).

In the INDI framework, actuator dynamics are not explicitly modeled, and state-dependent effects are typically neglected. This is often justified by assuming that these effects evolve slowly compared to actuator responses, as discussed in Sieberling et al. (2010). Under such assumptions, the closed-loop behavior of INDI effectively collapses to the actuator dynamics. While this is acceptable when all actuators exhibit similar dynamics, it becomes problematic in systems with heterogeneous actuator behavior, where differences in response speed can introduce unintended coupling and degraded performance.

The approach in Wang et al. (2019) attempts to account for state evolution across a single sampling interval, but this proves insufficient when actuator dynamics are significant, since the expected state change is not realized within one controller update. Likewise, the discrete-time method of Zhou et al. (2021) incorporates state-dependent terms but struggles when actuator time constants exceed the controller's time step, potentially causing excessive actuator commands and hidden oscillations.

Heterogeneous actuator dynamics are common in various systems and control strategies, especially with unconventional aircraft. One example is tilt-propellers, where the tilt mechanism has slower dynamics than the propeller (Bachler et al., 2025). Those are also found in airships (Cordeiro et al., 2022). Different actuator dynamics have also been observed between aerodynamic control surfaces and propellers (Raab et al., 2019). When a unified controller with the attitude angles as virtual inputs is used, as in De Ponti et al. (2025), Raab et al. (2018), the attitude dynamics are usually slower than the propeller dynamics.

The Variable Skew Quad Plane (VSQP) is a novel platform (Patent Diane & Remes, 2023) designed for precise landings in windy and dynamic conditions (De Ponti et al., 2025, 2023). In hover, it functions as a

* Corresponding author.
E-mail address: t.m.l.deponti@tudelft.nl (T. De Ponti).

https://doi.org/10.1016/j.conengprac.2026.106858
Received 17 October 2025; Received in revised form 19 January 2026; Accepted 16 February 2026
Available online 21 February 2026

quad-rotor using differential thrust for control, and transitions to forward flight where aerodynamic surfaces provide stability and a tail-mounted pusher propeller delivers propulsion. Unlike conventional quad-planes, its wing rotates by 90°, and the lateral rotors retract into the fuselage, improving cruise efficiency by reducing drag. In hover mode, the wing is stowed atop the fuselage, minimizing wind disturbance and enhancing control stability.

As part of the VSQP design optimization, it was found that the roll motors could be made smaller and lighter, given that the vehicle's inertia is primarily concentrated around the body-y and body-z axes. This modification reduces the overall weight of the drone, and the reduction of the propeller size leads to a decrease in the drag of the roll motors in forward flight. As a result, cruise efficiency and flight range are expected to improve. However, this configuration introduces non-uniform actuator dynamics, as the lighter roll motors respond faster than the larger, slower pitch motors. Consequently, a control strategy capable of managing these heterogeneous actuator dynamics was required.

One approach to consider the actuator dynamics independently of the higher-level control law is dynamic control allocation (Oppenheimer & Doman, 2004). Here, the actuator dynamics are directly inverted in the control allocation. On the other hand, the actuator dynamics compensation can be directly integrated in INDI, which was first proposed by Li et al. (2018) in 2018. It considers first- or second-order actuators by a scaling applied to the inputs computed by the control allocation. The work of Raab et al. (2019) then reformulates the INDI law and modifies the control effectiveness matrix used in the control allocation to account for the actuator dynamics (Steinert et al., 2025). This approach, called extended Incremental Nonlinear Dynamic Inversion (E-INDI), allows for the unification of different actuator dynamics and the specification of desired pseudo-control dynamics. The methods from Raab et al. (2019), Bhardwaj et al. (2021), and Steffensen et al. (2023) derive the INDI control law using an additional time derivative of the system output, thereby explicitly incorporating actuator dynamics into the effectiveness matrix itself. This refined control strategy, referred to as Actuator Nonlinear Dynamic Inversion (ANDI) in Steffensen et al. (2023), enhances compensation for actuator lag and improves overall system performance. The work of Steffensen et al. (2023) is extended to more generalized actuator dynamics in Liu et al. (2025). Another approach to consider actuator dynamics is to use an acceleration-based actuator control, which does not rely on the actuator position feedback but on acceleration feedback from the plant (Meyer-Brügel & Silvestre, 2024).

To incorporate actuator dynamics into incremental control laws, these dynamics must first be estimated. This has been demonstrated, for example, by Steffensen et al. (2024) for a fixed-wing model aircraft. However, such estimations are subject to uncertainty, which can affect the overall control performance. In Liu et al. (2025), the robustness and stability of ANDI were investigated, and the authors concluded that ANDI maintains satisfactory performance even in the presence of actuator bandwidth uncertainties. Furthermore, De Ponti et al. (2025) showed that ANDI continues to outperform INDI in systems with higher-order actuator dynamics approximated as first order, as verified through dynamic trajectory-tracking flight tests. However, it remains unclear at which point slow and/or different actuator dynamics make ANDI significantly more advantageous than INDI. Additionally, a general characterization of the fundamental limitations of INDI when applied to systems with heterogeneous actuator dynamics is needed.

The contributions of this paper are: (1) the derivation and application of a frequency-domain closed-loop response model to reveal the couplings introduced by applying INDI to a quadrotor system with heterogeneous and non-negligible actuator dynamics, and to analytically quantify their severity, identify the most affected axes, and determine the frequency ranges where they are most pronounced; (2) the first real-world flight test of ANDI on a quadrotor-like platform with heterogeneous motor dynamics, to the best of the authors' knowledge. This extends prior work from virtual to physical actuator heterogeneity and confirms that ANDI can eliminate coupling effects without degrading performance on uncoupled axes; (3) a comparative analysis of ANDI, INDI, and a lead-lag-augmented INDI designed to mitigate these effects; and (4) an extension of ANDI to account for actuator rate-induced control effects, such as the yawing moment generated by accelerating propeller inertia.

2. ANDI

Steffensen et al. (2023) introduced ANDI, an extension of the Nonlinear Dynamic Inversion (NDI) control law. It accounts for non-negligible first-order actuator dynamics, defined as:

$$\dot{\boldsymbol{u}} = \boldsymbol{\varepsilon}_{\boldsymbol{u}}\left(\boldsymbol{u}_{\boldsymbol{c}} - \boldsymbol{u}\right) = \boldsymbol{\varepsilon}_{\boldsymbol{u}}\Delta\boldsymbol{u}, \tag{1}$$

where $\boldsymbol{\varepsilon}_{\boldsymbol{u}} \in \mathbb{R}^{n_u \times n_u}$ is a diagonal matrix of the actuators' first-order corner frequencies, $\boldsymbol{u} \in \mathbb{R}^{n_u}$ represents the actuator states, and $\boldsymbol{u}_{\boldsymbol{c}} \in \mathbb{R}^{n_u}$ is the actuator command vector.

To derive the control law, we begin with a general system influenced by the actuator state and its time derivative. This dependency is especially relevant in applications such as quadrotor yaw control, where propeller-motor inertia can be non-negligible, as discussed in Smeur et al. (2016a). Additionally, we define the system output to be the time derivative of the state vector, such that:

$$\begin{aligned} \dot{\boldsymbol{x}} &= \boldsymbol{f}(\boldsymbol{x}, \boldsymbol{u}, \dot{\boldsymbol{u}}), \\ \boldsymbol{y} &= \dot{\boldsymbol{x}}, \end{aligned} \tag{2}$$

where $\boldsymbol{x} \in \mathbb{R}^{n_x}$ are the system's states and $\boldsymbol{y} \in \mathbb{R}^{n_y}$ are the outputs. Differentiating the system dynamics with respect to time yields:

$$\begin{aligned} \dot{\boldsymbol{y}} &= \frac{\partial \boldsymbol{f}(\boldsymbol{x}, \boldsymbol{u}, \dot{\boldsymbol{u}})}{\partial \boldsymbol{x}}\dot{\boldsymbol{x}} + \frac{\partial \boldsymbol{f}(\boldsymbol{x}, \boldsymbol{u}, \dot{\boldsymbol{u}})}{\partial \boldsymbol{u}}\dot{\boldsymbol{u}} + \frac{\partial \boldsymbol{f}(\boldsymbol{x}, \boldsymbol{u}, \dot{\boldsymbol{u}})}{\partial \dot{\boldsymbol{u}}}\ddot{\boldsymbol{u}} \\ &= \boldsymbol{F}_{\boldsymbol{x}}\dot{\boldsymbol{x}} + \boldsymbol{F}_{\boldsymbol{u}}\dot{\boldsymbol{u}} + \boldsymbol{F}_{\dot{\boldsymbol{u}}}\ddot{\boldsymbol{u}}, \end{aligned} \tag{3}$$

where $\boldsymbol{F}_{\boldsymbol{x}} \in \mathbb{R}^{n_x \times n_x}$, $\boldsymbol{F}_{\boldsymbol{u}} \in \mathbb{R}^{n_x \times n_u}$, and $\boldsymbol{F}_{\dot{\boldsymbol{u}}} \in \mathbb{R}^{n_x \times n_u}$. Applying the finite difference approximation $\ddot{\boldsymbol{u}} = f_s(1 - \exp(-s/f_s))\dot{\boldsymbol{u}}$ with sampling frequency f_s, along with the actuator dynamics from (1), leads to:

$$\begin{aligned} \dot{\boldsymbol{y}} &= \boldsymbol{F}_{\boldsymbol{x}}\dot{\boldsymbol{x}} + \boldsymbol{F}_{\boldsymbol{u}}\dot{\boldsymbol{u}} + \boldsymbol{F}_{\dot{\boldsymbol{u}}}f_s(1 - \exp(-s/f_s))\dot{\boldsymbol{u}}, \\ &= \boldsymbol{F}_{\boldsymbol{x}}\dot{\boldsymbol{x}} + \boldsymbol{F}_{\boldsymbol{u}}\dot{\boldsymbol{u}} + \boldsymbol{F}_{\dot{\boldsymbol{u}}}f_s\dot{\boldsymbol{u}} - \boldsymbol{F}_{\dot{\boldsymbol{u}}}f_s\exp(-s/f_s)\dot{\boldsymbol{u}}, \\ &= \boldsymbol{F}_{\boldsymbol{x}}\dot{\boldsymbol{x}} + \left(\boldsymbol{F}_{\boldsymbol{u}} + \boldsymbol{F}_{\dot{\boldsymbol{u}}}f_s\right)\dot{\boldsymbol{u}} - \boldsymbol{F}_{\dot{\boldsymbol{u}}}f_s\exp(-s/f_s)\dot{\boldsymbol{u}}, \\ &= \boldsymbol{F}_{\boldsymbol{x}}\dot{\boldsymbol{x}} + \left(\boldsymbol{F}_{\boldsymbol{u}} + \boldsymbol{F}_{\dot{\boldsymbol{u}}}f_s\right)\boldsymbol{\varepsilon}_{\boldsymbol{u}}\Delta\boldsymbol{u} - \boldsymbol{F}_{\dot{\boldsymbol{u}}}f_s\exp(-s/f_s)\boldsymbol{\varepsilon}_{\boldsymbol{u}}\Delta\boldsymbol{u}. \end{aligned} \tag{4}$$

To derive the control input, we set the pseudo-control vector $\boldsymbol{\nu} \in \mathbb{R}^{n_y}$ equal to $\dot{\boldsymbol{y}}$. Assuming $\left(\left[\boldsymbol{F}_{\boldsymbol{u}} + \boldsymbol{F}_{\dot{\boldsymbol{u}}}f_s\right]\boldsymbol{\varepsilon}_{\boldsymbol{u}}\right)$ is full rank, we apply its pseudoinverse to isolate $\Delta\boldsymbol{u}$, resulting in the ANDI control law:

$$\Delta\boldsymbol{u} = \left(\left[\boldsymbol{F}_{\boldsymbol{u}} + \boldsymbol{F}_{\dot{\boldsymbol{u}}}f_s\right]\boldsymbol{\varepsilon}_{\boldsymbol{u}}\right)^{+}\left(\boldsymbol{\nu} - \boldsymbol{F}_{\boldsymbol{x}}\dot{\boldsymbol{x}} + \boldsymbol{F}_{\dot{\boldsymbol{u}}}f_s e^{-s/f_s}\boldsymbol{\varepsilon}_{\boldsymbol{u}}\Delta\boldsymbol{u}\right). \tag{5}$$

In tracking the pseudo-control signal $\boldsymbol{\nu}$, actuators with faster dynamics, characterized by larger values of $\boldsymbol{\varepsilon}_{\boldsymbol{u}}$, receive smaller input commands compared to those with slower dynamics. This behavior naturally incorporates actuator dynamics into the control allocation, embedding them directly within the modified effectiveness matrix.

An alternative perspective on the operation of the ANDI control law becomes apparent in the special case where the number of actuators equals the number of controlled axes and $\left[\boldsymbol{F}_{\boldsymbol{u}} + \boldsymbol{F}_{\dot{\boldsymbol{u}}}f_s\right]\boldsymbol{\varepsilon}_{\boldsymbol{u}}$ is full rank, such that the pseudoinverse reduces to a true inverse. In this setting, ANDI first computes the required actuator rate $\dot{\boldsymbol{u}}$ to track the pseudo-control vector using the nominal INDI effectiveness matrix, and then derives the actual control increment $\Delta\boldsymbol{u}$ by scaling through ${\boldsymbol{\varepsilon}_{\boldsymbol{u}}}^{-1}$. This relationship becomes clear by expanding the inverse expression:

$$\left(\left[\boldsymbol{F}_{\boldsymbol{u}} + \boldsymbol{F}_{\dot{\boldsymbol{u}}}f_s\right]\boldsymbol{\varepsilon}_{\boldsymbol{u}}\right)^{-1} = {\boldsymbol{\varepsilon}_{\boldsymbol{u}}}^{-1}\left[\boldsymbol{F}_{\boldsymbol{u}} + \boldsymbol{F}_{\dot{\boldsymbol{u}}}f_s\right]^{-1}. \tag{6}$$

In this view, ANDI achieves tracking of the desired jerk input by regulating $\dot{\boldsymbol{u}}$, and subsequently mapping it through ${\boldsymbol{\varepsilon}_{\boldsymbol{u}}}^{-1}$ to produce actuator commands that inherently account for the dynamics of each actuator, resulting in a coordinated response.

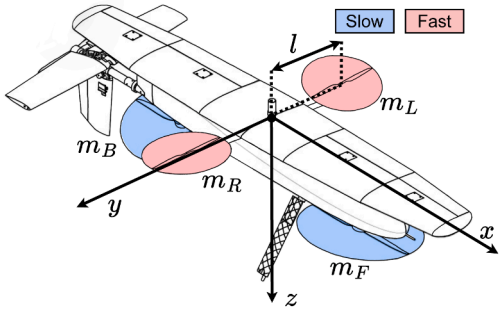

Fig. 1. Main actuators placement in VSQP during vertical flight.

3. INDI

A notable feature of the ANDI control law is that it generalizes the more specific INDI formulation. In fact, INDI can be directly derived from ANDI by assuming the actuators are infinitely fast, meaning that their dynamics can be neglected. For instance, in ANDI, the pseudo-control signal $\boldsymbol{\nu}$ can be computed linearly from the desired system output $\boldsymbol{y_d}$ and the current output $\boldsymbol{y}$ as:

$$\boldsymbol{\nu} = \boldsymbol{k_y}(\boldsymbol{y_d} - \boldsymbol{y}). \tag{7}$$

Different from Steffensen et al. (2023), to avoid pushing the actuators beyond their bandwidth, we propose that the set of gains $\boldsymbol{k_y}$ should be chosen to match the slowest actuator dynamics associated with each controlled output. In other words, $\boldsymbol{k_y} = \boldsymbol{\varepsilon_y}$, with:

$$\varepsilon_{y_i} = \min\left\{\varepsilon_{u_n} \mid G_{in} \neq 0\right\}, \tag{8}$$

where G_{in} denotes the entry $(i,n)^{\text{th}}$ of the control effectiveness matrix $\boldsymbol{G}$, indicating whether actuator u_n contributes to output y_i. This choice ensures that the controller respects the slowest relevant actuator dynamics, avoiding over-aggressive commands. Substituting this into (5) and rearranging terms yields:

$$\begin{aligned}\boldsymbol{\Delta u} = &\left(\left[\boldsymbol{F_u} + \boldsymbol{F_{\dot u}} f_s\right]\boldsymbol{\varepsilon_u}\right)^{+}\left(\boldsymbol{\varepsilon_y}(\boldsymbol{y_d} - \dot{\boldsymbol{x}}) + \boldsymbol{F_{\dot u}} f_s \exp(-s/f_s)\boldsymbol{\varepsilon_u}\boldsymbol{\Delta u}\right)\\ &+ \left(\left[\boldsymbol{F_u} + \boldsymbol{F_{\dot u}} f_s\right]\boldsymbol{\varepsilon_u}\right)^{+}\left(-\boldsymbol{F_x}\dot{\boldsymbol{x}}\right).\end{aligned} \tag{9}$$

Letting $\boldsymbol{\varepsilon_u} \to \infty$, and consequently $\boldsymbol{\varepsilon_y} \to \infty$, while substituting the desired output $\boldsymbol{y_d}$ with the INDI pseudo-control signal $\boldsymbol{\vartheta}$, yields the nominal and familiar INDI control law, as defined for example in Smeur et al. (2016a):

$$\boldsymbol{\Delta u} = \left(\left[\boldsymbol{F_u} + \boldsymbol{F_{\dot u}} f_s\right]\right)^{+}\left(\boldsymbol{\vartheta} - \dot{\boldsymbol{x}} + \boldsymbol{F_{\dot u}} f_s \exp(-s/f_s)\boldsymbol{\Delta u}\right). \tag{10}$$

This derivation is important because it clearly identifies the assumptions behind the INDI control law. In particular, it shows that INDI ignores state-dependent terms and actuator dynamics. Some earlier approaches, such as Smeur et al. (2016a), rely on the time-scale separation principle to justify this simplification. However, this assumption is often difficult to validate in practice. ANDI does not rely on time-scale separation and therefore offers a clearer and more grounded understanding of the conditions under which INDI may be expected to perform well.

In ANDI, including state-dependent terms is optional and can be leveraged if such effects are known or significant. For the purpose of this study, and to isolate and clarify the specific impact of ignoring actuator dynamics, we assume these state-dependent terms to be negligible. This is a reasonable simplification in scenarios such as quadcopter flight at low airspeeds, where these effects are typically minor.

4. System model

To highlight how neglecting actuator dynamics can degrade control performance, and how ANDI addresses this issue, we begin with the definition of the model of the modified VSQP. As shown in Fig. 1, the VSQP has two distinct motor types: one with fast dynamics and one with slow dynamics. The two motors controlling the pitch axis have slow dynamics (large propeller diameter), while the two motors responsible for roll control have fast dynamics (small propeller diameter).

We aim to stabilize the system by controlling, in order, the body z-axis acceleration a_z, and the roll, pitch, and yaw angular accelerations $\dot p$, $\dot q$, and $\dot r$. Control is achieved using the four quadrotor motors, ordered as m_F, m_R, m_B, and m_L (front, right, back, and left). This results in the following model:

$$\boldsymbol{J} = \begin{bmatrix} m^{-1} & 0 & 0 & 0 \\ 0 & I_{xx}^{-1} & 0 & 0 \\ 0 & 0 & I_{yy}^{-1} & 0 \\ 0 & 0 & 0 & I_{zz}^{-1} \end{bmatrix}, \tag{11}$$

$$\boldsymbol{F_u} = \boldsymbol{J}\begin{bmatrix} -k_1 & -k_2 & -k_1 & -k_2 \\ 0 & -lk_2 & 0 & lk_2 \\ lk_1 & 0 & -lk_1 & 0 \\ \tau_1 & -\tau_2 & \tau_1 & -\tau_2 \end{bmatrix}, \tag{12}$$

$$\boldsymbol{F_{\dot u}} = \boldsymbol{J}\begin{bmatrix} 0 & 0 & 0 & 0 \\ 0 & 0 & 0 & 0 \\ 0 & 0 & 0 & 0 \\ \beta_1 & -\beta_2 & \beta_1 & -\beta_2 \end{bmatrix}, \tag{13}$$

$$\boldsymbol{\varepsilon_u} = \begin{bmatrix} \varepsilon_1 & 0 & 0 & 0 \\ 0 & \varepsilon_2 & 0 & 0 \\ 0 & 0 & \varepsilon_1 & 0 \\ 0 & 0 & 0 & \varepsilon_2 \end{bmatrix}, \tag{14}$$

$k_i,\ \tau_i,\ \beta_i,\ \varepsilon_i, l \in \mathbb{R}_{>0}$,

where m is the mass of the drone, I is the inertia tensor of the drone assumed to be purely diagonal, l is the moment arm of the motors about the centre of gravity, k is the linear coefficient relating motor state to thrust force, τ is the linear coefficient relating motor state to torque, and β is the linear coefficient relating the rate of change of the motor state to torque.

While this setup is no more complex than a standard quadrotor control model, it is essential to note that the actuators controlling roll and those controlling pitch each have identical dynamics within their respective pairs. However, the roll and pitch actuators differ from each other, with one pair having fast dynamics and the other slow. Consequently, properly handling the mixing of these differing dynamics is essential for thrust and yaw control, which rely on coordinated contributions from both actuator types.

Table 1[1] summarizes the key parameters of the VSQP model, as identified through flight tests and static test-bench experiments. The VSQP operates with 6s LiPo batteries, and the parameters reported in Table 1 are estimated at the nominal battery operating range, between 4.2 and 3.8 volts per cell.

Actuator dynamics are identified using a series of static tests conducted on a motor test bench. Step command inputs of varying magnitudes are applied to the ESC-motor assembly, while an optical probe measures the motor's rotational speed. The actuator dynamics corner frequency is then estimated as the value that minimizes the sum of squared errors between the model response and the measured rotational speed across the entire dataset. The changes in actuator dynamics due to voltage drop in the nominal operating range of the batteries are assumed to be negligible. To allow the larger pitch motors to carry most of the drone's weight while preserving yaw balance, the smaller roll motors are slightly tilted to enhance their yaw effectiveness.

[1] *pprz* is the actuator state unit in the employed autopilot flight system Paparazzi UAV, ranging from 0 to 9600.

Table 1
Parameters of the VSQP model.

Term	Value	Unit
m	6.67	kg
I_{xx}	1.29×10^{-1}	kg m^2
I_{yy}	9.50×10^{-1}	kg m^2
I_{zz}	1.28	kg m^2
l	4.23×10^{-1}	m
ε_1	22.0	rad s^{-1}
ε_2	29.0	rad s^{-1}
k_1	5.85×10^{-4}	m s^{-2} pprz^{-1}
k_2	2.11×10^{-4}	m s^{-2} pprz^{-1}
τ_1	1.17×10^{-4}	rad s^{-2} pprz^{-1}
τ_2	2.01×10^{-4}	rad s^{-2} pprz^{-1}
β_1	2.10×10^{-5}	rad s^{-1} pprz^{-1}
β_2	2.34×10^{-6}	rad s^{-1} pprz^{-1}

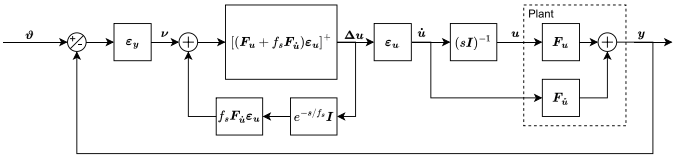

Fig. 2. ANDI innerloop control diagram.

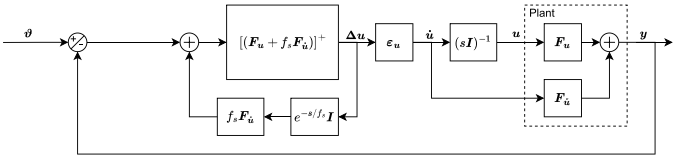

Fig. 3. INDI innerloop control diagram.

5. Closed loop analysis

To understand the effect of differing actuator dynamics, we now study the loop structure and transfer function of both ANDI and INDI. The control diagrams for the quadrotor controlled using ANDI and INDI are presented in Figs. 2 and 3, respectively.

In Fig. 2, $\boldsymbol{\varepsilon_y}$ is a diagonal matrix of gains chosen according to Eq. (8) :

$$\boldsymbol{\varepsilon_y} = \begin{bmatrix} \varepsilon_T & 0 & 0 & 0 \\ 0 & \varepsilon_\phi & 0 & 0 \\ 0 & 0 & \varepsilon_\theta & 0 \\ 0 & 0 & 0 & \varepsilon_\psi \end{bmatrix} = \begin{bmatrix} \varepsilon_1 & 0 & 0 & 0 \\ 0 & \varepsilon_2 & 0 & 0 \\ 0 & 0 & \varepsilon_1 & 0 \\ 0 & 0 & 0 & \varepsilon_1 \end{bmatrix}. \tag{15}$$

In both control loops, the following assumptions are adopted: (1) the absence of external disturbances; (2) perfect model knowledge; and (3) a negligible state-dependent term, justified by the quadcopter operating at low airspeeds. For clarity, an additional assumption is introduced: (4) $\boldsymbol{F_{\dot{u}}}$ is negligible, since the inertia of the motor–propeller assembly is small compared to the inertia about the body z-axis of the VSQP, and the dominant contribution to yaw control arises from propeller drag. This assumption simplifies the analysis and keeps the formulation general, allowing the results to apply to actuators with different dynamics beyond the motor-propeller case considered here, such as servos.

For both control loops, using the forward path transfer function matrix $\boldsymbol{A}(s)$, we can compute the closed-loop transfer function matrix $(\boldsymbol{I} + \boldsymbol{A}(s))^{-1}\boldsymbol{A}(s)$, which is a 4×4 mapping from the desired output vector $\boldsymbol{\vartheta}$ to the actual output $\boldsymbol{y}$. The full derivation can be found at De Ponti et al. (4TU.ResearchData, 2025). For ANDI(A) and INDI(I), we obtain:

$$\frac{\boldsymbol{y}}{\boldsymbol{\vartheta}}(s)_{\mathrm{A}} = \begin{bmatrix} \frac{\varepsilon_1}{s+\varepsilon_1} & 0 & 0 & 0 \\ 0 & \frac{\varepsilon_2}{s+\varepsilon_2} & 0 & 0 \\ 0 & 0 & \frac{\varepsilon_1}{s+\varepsilon_1} & 0 \\ 0 & 0 & 0 & \frac{\varepsilon_1}{s+\varepsilon_1} \end{bmatrix}, \tag{16}$$

$$\frac{\boldsymbol{y}}{\boldsymbol{\vartheta}}(s)_{\mathrm{I}} = \begin{bmatrix} \frac{\sigma_2}{\sigma_1} & 0 & 0 & \frac{I_{zz}}{m}\frac{\sigma_4}{\sigma_1} \\ 0 & \frac{\varepsilon_2}{s+\varepsilon_2} & 0 & 0 \\ 0 & 0 & \frac{\varepsilon_1}{s+\varepsilon_1} & 0 \\ \frac{m}{I_{zz}}\frac{\sigma_5}{\sigma_1} & 0 & 0 & \frac{\sigma_3}{\sigma_1} \end{bmatrix}, \tag{17}$$

where:

$$\sigma_1 = (s+\varepsilon_1)(s+\varepsilon_2)(k_1\tau_2 + k_2\tau_1),$$
$$\sigma_2 = (k_1\tau_2\varepsilon_1 + k_2\tau_1\varepsilon_2)s + (k_1\tau_2 + k_2\tau_1)\varepsilon_1\varepsilon_2,$$
$$\sigma_3 = (k_2\tau_1\varepsilon_1 + k_1\tau_2\varepsilon_2)s + (k_1\tau_2 + k_2\tau_1)\varepsilon_1\varepsilon_2,$$
$$\sigma_4 = k_1k_2(\varepsilon_1 - \varepsilon_2)s,$$
$$\sigma_5 = \tau_1\tau_2(\varepsilon_1 - \varepsilon_2)s.$$

The ANDI closed-loop transfer function exhibits a first-order response along all axes, governed by the selected values of $\boldsymbol{\varepsilon_y}$, with no coupling between axes. This decoupled behavior is achieved by explicitly inverting the actuator dynamics within the control law itself.

The same is not true for the INDI closed-loop transfer function across all axes. As expected, the roll and pitch axes, each controlled by actuators with identical dynamics, display clean first-order responses, with corner frequencies determined by the dynamics of the corresponding actuators.

In contrast, the thrust and yaw axes exhibit notable differences. Their transfer function matrices contain nonzero off-diagonal terms, indicating coupling between these two axes. Moreover, their response is second-order instead of first-order. The poles of these responses align with the actuator time constants, reflecting a dynamic mix of both fast and slow actuators being driven to their limits.

5.1. Diagonal entries

The diagonal entries of the closed-loop transfer function matrix describe the direct relationship between a desired input on one axis and its corresponding output. From Eq. (17), we observe that these transfer functions take the form of second-order systems with a zero, of which we will show that it always lies between the two poles. Consider the transfer function from the desired to actual yaw angular acceleration (the same structure holds for other diagonal entries). It can be rearranged as:

$$\begin{aligned} \frac{\boldsymbol{y}}{\boldsymbol{\vartheta}}(s)_{\mathrm{I}_{(4,4)}} &= \frac{(k_2\tau_1\varepsilon_1 + k_1\tau_2\varepsilon_2)s + (k_1\tau_2 + k_2\tau_1)\varepsilon_1\varepsilon_2}{(s+\varepsilon_1)(s+\varepsilon_2)(k_1\tau_2 + k_2\tau_1)}, \\ &= K \cdot \frac{(k_2\tau_1\varepsilon_1 + k_1\tau_2\varepsilon_2)s + (k_1\tau_2 + k_2\tau_1)\varepsilon_1\varepsilon_2}{(s+\varepsilon_1)(s+\varepsilon_2)}. \end{aligned} \tag{18}$$

The zero of this transfer function is located at:

$$z = -\frac{(k_1\tau_2 + k_2\tau_1)\varepsilon_1\varepsilon_2}{k_2\tau_1\varepsilon_1 + k_1\tau_2\varepsilon_2}. \tag{19}$$

Assuming without loss of generality that $\varepsilon_2 > \varepsilon_1$, the zero can lie outside the range defined by the poles only if one of the following holds:

Case 1: $z < -\varepsilon_2$, which requires

$$\frac{(k_1\tau_2 + k_2\tau_1)\varepsilon_1}{k_2\tau_1\varepsilon_1 + k_1\tau_2\varepsilon_2} > 1, \tag{20}$$

but this is false since the denominator is strictly greater than the numerator for $k_i, \tau_i, \varepsilon_i \in \mathbb{R}_{>0}$.

Case 2: $z > -\varepsilon_1$, which requires

$$\frac{(k_1\tau_2 + k_2\tau_1)\varepsilon_2}{k_2\tau_1\varepsilon_1 + k_1\tau_2\varepsilon_2} < 1, \tag{21}$$

which is also false, as the numerator exceeds the denominator.

We therefore conclude that the zero must lie strictly between the two poles:

The magnitude plot of $\frac{\boldsymbol{y}}{\boldsymbol{\vartheta}}(s)_{\mathrm{I}_{(4,4)}}$ for the sample system presented in Table 1 is shown in Fig. 4, where it is compared to the first-order response dynamics of the two actuator types.

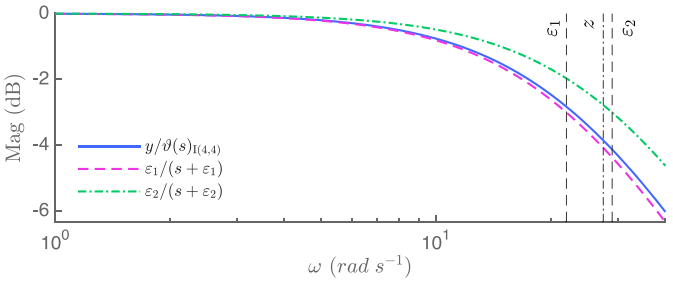

Fig. 4. Magnitude plot comparison between the diagonal transfer function $\frac{y}{\vartheta}(s)_{I_{(4,4)}}$ for the sample system of Table 1 and first-order responses.

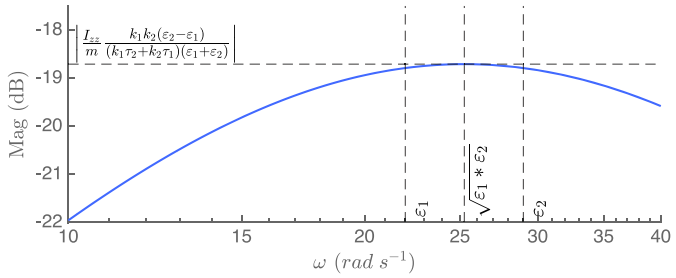

Fig. 5. Magnitude plot of the off-diagonal transfer function $\frac{y}{\vartheta}(s)_I(1,4)$ for the sample system of Table 1.

Since the zero lies between the two poles, the system's gain and phase response are bounded between those of first-order systems with corner frequencies ε_1 and ε_2. The resulting behavior is slightly faster than the slowest actuator but slower than the fastest one.

5.2. Off-diagonal entries

In contrast to the diagonal entries, the off-diagonal entries of the closed-loop transfer function matrix, which represent coupling between axes, exhibit a more interesting magnitude response. Consider, for example, the transfer function from a desired yaw acceleration to the body z-axis acceleration. This term, $\frac{y}{\vartheta}(s)_{I_{(1,4)}}$, has the following structure:

$$\begin{aligned}\frac{y}{\vartheta}(s)_{I_{(1,4)}} &= \frac{I_{zz}k_1k_2(\varepsilon_1-\varepsilon_2)s}{m(s+\varepsilon_1)(s+\varepsilon_2)(k_1\tau_2+k_2\tau_1)},\\ &= \frac{I_{zz}}{m}\frac{k_1k_2(\varepsilon_1-\varepsilon_2)}{k_1\tau_2+k_2\tau_1}\cdot\frac{s}{(s+\varepsilon_1)(s+\varepsilon_2)},\\ &= K\cdot\chi(s).\end{aligned} \tag{22}$$

This transfer function has the same two poles as the diagonal entries, located at the actuator dynamics ε_1 and ε_2, but also introduces a zero at the origin. As a result, the magnitude response starts from zero at low frequencies, rises to a peak, flattens near the lower actuator corner frequency, and rolls off again after the higher actuator frequency. This "peak-like" shape is particularly relevant for analyzing the severity and frequency range of coupling effects.

We examine the magnitude of the term $\chi(s)$ to identify the frequency at which this peak occurs. First, we compute its magnitude:

$$\begin{aligned}|\chi(j\omega)| &= \left|\frac{j\omega}{(j\omega+\varepsilon_1)(j\omega+\varepsilon_2)}\right|,\\ &= \frac{\omega}{\sqrt{\omega^2+\varepsilon_1^2}\sqrt{\omega^2+\varepsilon_2^2}}.\end{aligned} \tag{23}$$

To find the peak frequency, we analyze the squared magnitude, which peaks at the same frequency:

$$|\chi(j\omega)|^2 = \frac{\omega^2}{(\omega^2+\varepsilon_1^2)(\omega^2+\varepsilon_2^2)}. \tag{24}$$

Letting $a=\omega^2$, we compute the derivative with respect to a:

$$\begin{aligned}\frac{d|\chi(j\omega)|^2}{da} &= \frac{1}{(a+\varepsilon_1^2)(a+\varepsilon_2^2)}\\ &- \frac{a}{(a+\varepsilon_1^2)^2(a+\varepsilon_2^2)} - \frac{a}{(a+\varepsilon_1^2)(a+\varepsilon_2^2)^2},\\ &= \frac{(a+\varepsilon_1^2)(a+\varepsilon_2^2)-a[(a+\varepsilon_1^2)+(a+\varepsilon_2^2)]}{(a+\varepsilon_1^2)^2(a+\varepsilon_2^2)^2},\\ &= \frac{\varepsilon_1^2\varepsilon_2^2-a^2}{(a+\varepsilon_1^2)^2(a+\varepsilon_2^2)^2},\end{aligned} \tag{25}$$

and solve for the numerator equal to zero to find the peak frequency:

$$a_p=\varepsilon_1\varepsilon_2 \quad\Rightarrow\quad \omega_p=\sqrt{\varepsilon_1\varepsilon_2}. \tag{26}$$

This frequency corresponds to the geometric mean of the two actuator dynamics. To compute the peak magnitude, we substitute ω_p back into the magnitude expression:

$$\begin{aligned}\left|\frac{y}{\vartheta}(j\omega_p)_I(1,4)\right| &= |K|\cdot|\chi(j\omega_p)|,\\ &= \left|\frac{I_{zz}}{m}\frac{k_1k_2(\varepsilon_1-\varepsilon_2)}{k_1\tau_2+k_2\tau_1}\right|\cdot\frac{\sqrt{\varepsilon_1\varepsilon_2}}{\sqrt{\varepsilon_1\varepsilon_2+\varepsilon_1^2}\sqrt{\varepsilon_1\varepsilon_2+\varepsilon_2^2}},\\ &= \left|\frac{I_{zz}}{m}\frac{k_1k_2(\varepsilon_1-\varepsilon_2)}{k_1\tau_2+k_2\tau_1}\right|\frac{1}{\varepsilon_1+\varepsilon_2},\\ &= \left|\frac{I_{zz}}{m}\frac{k_1k_2(\varepsilon_1-\varepsilon_2)}{(k_1\tau_2+k_2\tau_1)(\varepsilon_1+\varepsilon_2)}\right|.\end{aligned} \tag{27}$$

The magnitude plot of this transfer function for the sample system depicted by Table 1 is shown in Fig. 5. These insights are powerful, as they imply that in systems with heterogeneous actuator dynamics, it is possible to anticipate to what extent the INDI controller will amplify coupling effects, based solely on some physical parameters and the effectiveness matrix.

In practical terms, when INDI is used within a larger outer-loop controller, such as for attitude stabilization, this analysis allows us to predict whether heterogeneity in actuator dynamics might introduce frequency bands with amplification effects.

Finally, from Eq. (17), we can also observe that if the effectiveness matrix is biased toward one axis, for instance, if $|k_1k_2| \gg |\tau_1\tau_2|$, then the most significant coupling occurs in the transfer function from the desired input on the less effectively actuated axis to the output on the more effectively actuated axis. This is because the gain of the off-diagonal transfer function is proportional to the ratio between the product of the effectiveness terms for the output axis and the determinant of the effectiveness matrix.

In other words, when tracking a desired signal along an axis that demands a high actuator effort, any allocation inaccuracies tend to propagate and become more visible along axes with stronger control authority. In the case of a standard quadrotor, this insight highlights the importance of analyzing the coupling from a desired yaw acceleration (which is weakly actuated) to the body z-axis acceleration (which is strongly actuated).

Using the values of Table 1, together with the results of Eqs. (26) and (27), we estimate that the most significant coupling, specifically from yaw angular acceleration to body z-axis acceleration, occurs at approximately $25.3\,\mathrm{rad\,s^{-1}}$, with a peak magnitude of 1.19×10^{-1}, as also confirmed by Fig. 5. This analysis suggests that, although some coupling exists, it is not expected to be severe, since the actuator dynamics are still relatively similar and fast.

Nevertheless, due to the omission of actuator dynamics in the control allocation process under INDI, a step input in yaw acceleration should still induce a measurable response in the body z-axis acceleration.

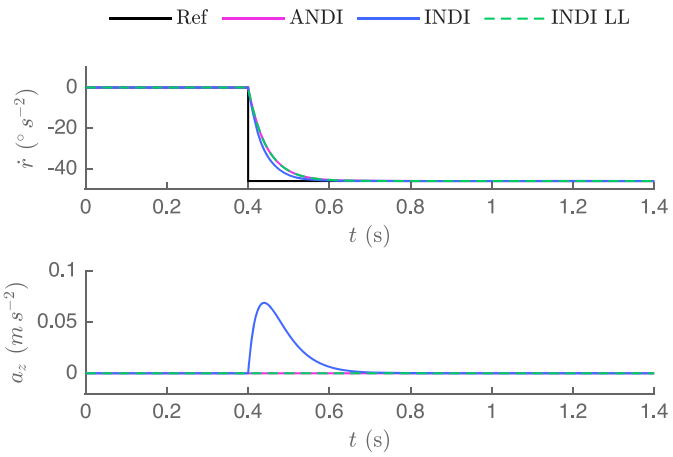

Fig. 6. Simulation results for a yaw angular acceleration step input.

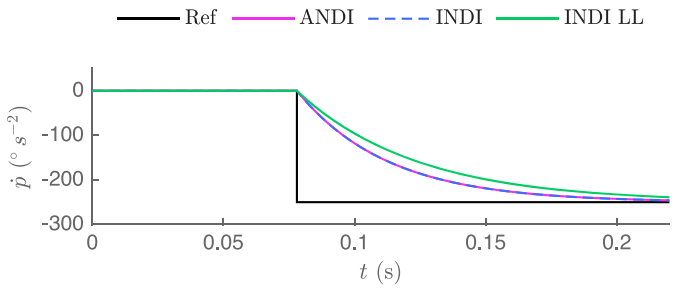

Fig. 7. Simulation results for a roll angular acceleration step input.

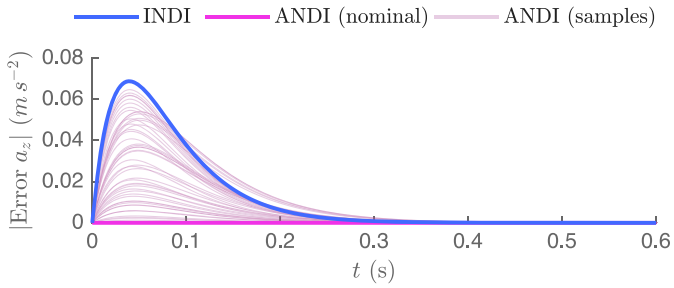

Fig. 8. Step response from yaw to vertical acceleration (a_z). The shaded magenta curves represent uncertain ANDI system realizations with uncertainty on ϵ_2 of up to 25%, while the solid blue and magenta lines correspond to the INDI and nominal ANDI responses, respectively. (For interpretation of the references to colour in this figure legend, the reader is referred to the web version of this article.)

6. Lead lag INDI

A key structural property emerges when the actuator dynamics are identical. Specifically, if $(\epsilon_1 - \epsilon_2) = 0$, then the off-diagonal transfer function entries vanish, and the diagonal entries reduce to first-order systems with a common corner frequency equal to the shared actuator rate. This result is expected and aligns with observations from the decoupled roll and pitch axes.

This raises an important question: Is artificially slowing down the fast actuators to match the slow ones a viable solution? Such an approach would involve inserting a lead-lag filter in front of the actuator dynamics block for the fast motors, with the structure:

$$H(s) = \frac{\epsilon_1}{s+\epsilon_1} \cdot \frac{s+\epsilon_2}{\epsilon_2}. \tag{28}$$

This filter effectively cancels the fast actuator dynamics and replaces them with those of the slower actuators. We refer to this strategy as Lead Lag Incremental Nonlinear Dynamic Inversion (LL-INDI). While it successfully eliminates coupling between axes, it comes at the cost of two significant drawbacks:

1. Since this approach can only be applied uniformly across all controlled axes, it unnecessarily slows down dynamics on already decoupled axes, such as roll and pitch in the sample system.
2. It degrades saturation handling performance, since the filter is applied after control allocation, and the control allocation algorithm remains unaware of its effect.

In contrast, ANDI avoids these issues. It preserves fast response on decoupled axes and offers the flexibility to explicitly manage actuator saturation, such as through a Weighted Least Squares (WLS) control allocation method (Smeur et al., 2017), directly within the allocation stage.

7. Simulation study

To verify the conclusions drawn from the closed-loop analysis, we perform simulations of the VSQP under three controllers: ANDI, INDI, and LL-INDI. All simulation files and flight test data are available at De Ponti et al. (4TU.ResearchData, 2025). The first test consists of a step input in yaw acceleration, while simultaneously requiring zero body z-axis acceleration.

Fig. 6 shows that initially, INDI responds more quickly due to its pole associated with the faster actuator dynamics. However, all controllers converge to the desired yaw acceleration in approximately the same amount of time. A notable difference is the clear positive peak observed in the body z-axis acceleration under INDI. This peak results from neglecting actuator dynamics: as the fast motors quickly decrease thrust and the slower motors fail to increase thrust equally fast, total thrust temporarily drops. This imbalance induces a downward acceleration, deviating from the zero body z-axis acceleration requirement. As expected, LL-INDI behaves identically to ANDI on coupled axes, since the fast actuator dynamics have been filtered to match the slow ones.

When we evaluate the performance on the uncoupled roll axis by commanding a step input in roll angular acceleration, as shown in Fig. 7, both ANDI and INDI converge rapidly, following the fast actuator dynamics. In contrast, LL-INDI lags behind due to the imposed filtering, which unnecessarily slows down the response even on this decoupled axis.

The difference in this case is small due to the relatively similar actuator dynamics of the modified VSQP. However, as the disparity in actuator dynamics increases, the slowing effect introduced by LL-INDI will become more pronounced.

7.1. Sensitivity analysis

Previous works have addressed the robustness of ANDI with respect to model inaccuracies and approximations. Like INDI, ANDI is an incremental control law and therefore exhibits good robustness margins against disturbances, which it incrementally compensates for.

However, modeling actuators as ideal first-order systems with known corner frequencies is often inaccurate in practice. Such model mismatches can degrade the performance of the ANDI control loop. In the case of the VSQP platform, it was observed that while the first-order assumption remains a reasonable approximation, the corner frequency is not constant–it varies, particularly depending on motor spin-up or spin-down. This motivates a sensitivity analysis of ANDI performance with respect to uncertainties in actuator corner frequencies.

In Fig. 8, we compare the body z-axis acceleration response to a step in desired yaw acceleration for INDI and a set of Monte Carlo simulations of an uncertain ANDI system. The uncertainty is introduced as up to 25% variation in the value of ϵ_2 used within the inversion of the ANDI control law. Results show that, in the worst-case realizations, a 25% mismatch

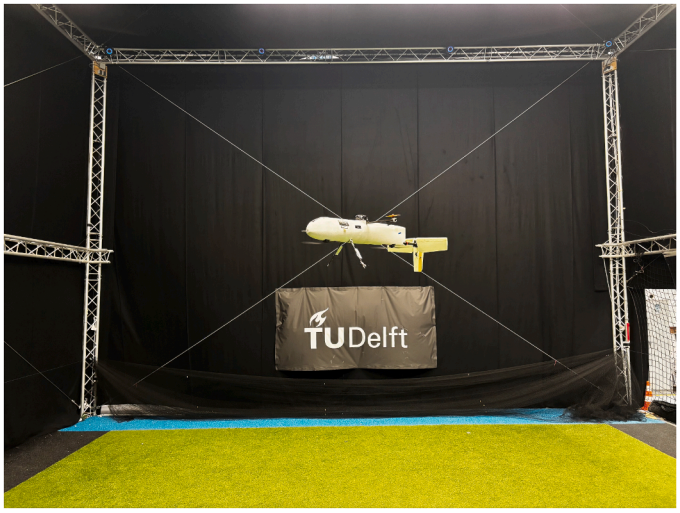

Fig. 9. The VSQP hovering in the indoor test facility of TuDelft.

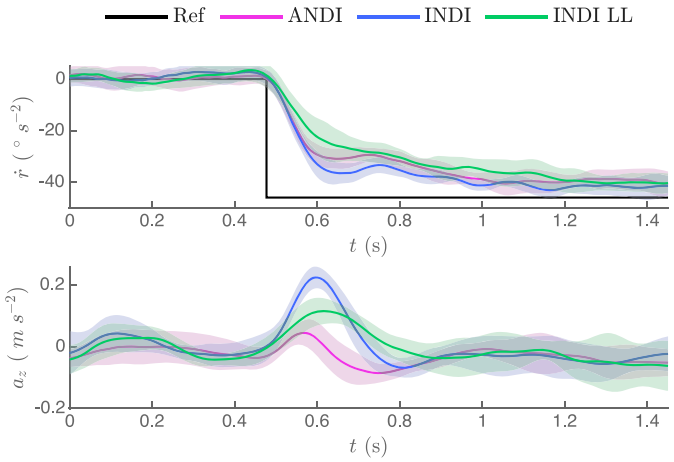

Fig. 10. Flight test results for a yaw angular acceleration step input. The lines are the average of 10 repetitions, and the shaded areas indicate one standard deviation. The signals are post-processed using a second-order Butterworth filter ($40, \mathrm{rad\,s^{-1}}$ cutoff), applied forward and backward to eliminate phase delay.

is sufficient to nullify the performance advantage of ANDI over INDI, resulting in comparable deviations from equilibrium. This highlights that although ANDI provides a theoretically robust solution, its practical effectiveness relies on reasonably accurate actuator modeling–especially in systems like the VSQP, where actuator dynamics are already relatively fast and similar, making performance differences more difficult to detect.

8. Real-world flight test

To validate the conclusions in a real-world setting, hovering tests were conducted at TU Delft's indoor flight facility using the VSQP, shown in Fig. 9. The tested platform features the same heterogeneous actuator dynamics as those analyzed in simulation. An additional minor difference from the nominal VSQP is the absence of the wing, as the system is still in the prototyping phase; however, this has no impact on hovering performance.

The same tests performed in simulation were replicated in flight. Each test was repeated 10 times per controller, and the mean and standard deviation at each time step were recorded. To mitigate noise in acceleration signals arising from real-world sensors, all signals in the control laws are synchronously filtered using identical filters across all tested controllers, following Smeur et al. (2016a). To further ensure comparability, the batteries are fully charged before each experiment to maintain the same supply voltage across all tests. Fig. 10 shows the results of the yaw acceleration step input experiment.

Naturally, some discrepancies arise between simulation and reality. The measured signals are noisier, and the system does not converge to the step input as cleanly. These deviations can be attributed to model mismatch and unmodeled physical effects.

For instance, the VSQP features a vertical tail, which generates an increasing counteracting aerodynamic moment as the vehicle's yaw rate increases. Despite these complexities, the core observation remains valid: under INDI, a distinct peak appears in the body z-axis acceleration, even more pronounced than in simulation, clearly indicating dynamic coupling in real flight conditions. In contrast, although less cleanly than in simulation, both ANDI and LL-INDI do not exhibit such a pronounced peak. Their body z-axis acceleration remains largely unaffected, with the average downward acceleration peak in ANDI being only 18% of that observed in INDI, demonstrating effective decoupling in practice. The small discrepancy with respect to the simulation results can be attributed to minor modeling inaccuracies in the effectiveness matrix and to the assumption that the actuators behave as perfect first-order systems. While this assumption is largely valid under smooth and

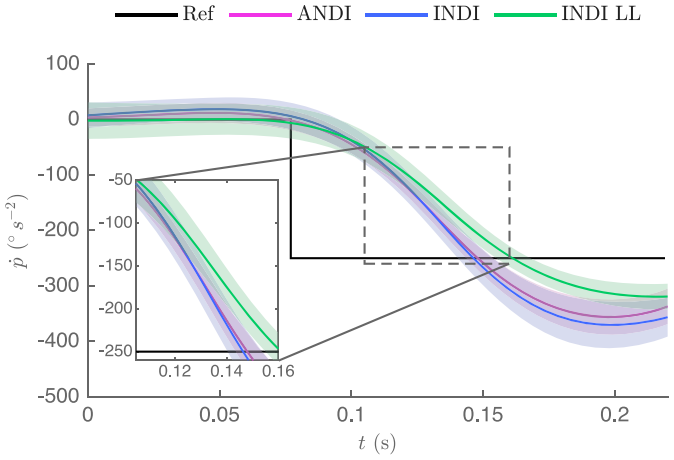

Fig. 11. Flight test results for a yaw angular acceleration step input. The lines average 10 repetitions, and the shaded areas indicate one standard deviation. The signals are post-processed using a second-order Butterworth filter ($40, \mathrm{rad\,s^{-1}}$ cutoff), applied forward and backward to eliminate phase delay.

continuous operation, it becomes inaccurate when tracking step inputs, as actuators cannot accelerate infinitely fast. This leads to a transient mismatch at the onset of the maneuver, which in turn causes the small peak observed in ANDI and LL-INDI.

Fig. 11 presents the result for the roll acceleration step input test.

Also in this case, some discrepancies arise compared to the simulation. In particular, all controllers deviate from a perfect first-order response and, for instance, exhibit overshoot. This is due to unmodeled discrepancies, such as inaccuracies in roll effectiveness modeling. Nonetheless, the core conclusion remains valid, as ANDI and INDI show very similar responses, whereas LL-INDI clearly lags behind.

9. Conclusion

In conclusion, applying standard INDI to systems with heterogeneous actuator dynamics leads to undesired coupling between controlled axes. The severity of this coupling can be estimated a priori based on the actuator dynamics and the control effectiveness matrix. These coupling effects become more pronounced as the difference between actuator dynamics increases, and as the overall actuator bandwidth decreases.

In contrast, ANDI, in addition to enabling compensation for state-induced disturbances (when modeled), directly inverts actuator dynamics within the control allocation stage, effectively eliminating axis coupling at its source. However, its effectiveness depends on having a reasonably accurate model of the actuator dynamics, which represents an additional requirement compared to INDI, as it introduces a dependency on model knowledge that INDI typically avoids.

While modifications such as LL-INDI can be applied to mitigate coupling in INDI, this approach has notable drawbacks differently from ANDI: it unnecessarily slows down the response of otherwise decoupled axes, impairs saturation handling, since the control allocation algorithm is unaware of the lead-lag filters, and increases controller complexity overall.

This paper investigated a system with heterogeneous actuator dynamics that, while not identical, were still relatively similar in bandwidth. Future work should explore the effectiveness of ANDI in systems with more extreme differences in actuator dynamics, where the benefits and limitations of inverting the actuator dynamics may become more pronounced. One such example is tilt-rotor systems, in which slower servos must be coordinated with significantly faster motors. Additionally, the current study assumes linear, time-invariant actuator behavior without saturation. A valuable extension would be to assess the performance and robustness of ANDI in the presence of actuator nonlinearities, time-varying dynamics, and saturation. Understanding how ANDI handles these practical challenges is essential for extending its applicability to more demanding control scenarios.

CRediT authorship contribution statement

Tomaso De Ponti: Writing – review & editing, Writing – original draft, Visualization, Validation, Software, Methodology, Investigation, Formal analysis, Data curation, Conceptualization; **Simon Hafner:** Writing – review & editing, Methodology, Investigation, Formal analysis, Conceptualization; **Ewoud Smeur:** Writing – review & editing, Supervision, Methodology, Conceptualization; **Bart Remes:** Supervision, Project administration, Funding acquisition.

Declaration of competing interest

The authors declare that they have no known competing financial interests or personal relationships that could have appeared to influence the work reported in this paper.

Acknowledgment

This research was co-funded by the Royal Dutch Navy and the Dutch Coast Guard. This initiative aims to foster collaboration and innovation in maritime endeavors. Simon Hafner is supported by a scholarship from Munich Aerospace e.V.

References

Bachler, J., Steinert, A., Hafner, S., & Holzapfel, F. (2025). Jerk-based control allocation for aerial vehicles with tilting rotors. *ASME Letters in Dynamic Systems and Control (LDSC)*. https://doi.org/10.1115/1.4070054

Bhardwaj, P., Raab, S. A., & Holzapfel, F. (2021). Higher order reference model for continuous dynamic inversion control. In *AIAA Scitech 2021 forum*. https://doi.org/10.2514/6.2021-1130

Cordeiro, R. A., Marton, A. S., Azinheira, J. R., Carvalho, J. R. H., & Moutinho, A., et al. (2022). Increased robustness to delay in incremental controllers using input scaling gain. *IEEE Transactions on Aerospace and Electronic Systems*, *58*(2), 1199–1210. https://doi.org/10.1109/TAES.2021.3123215

De Ponti, T. M. L., Hafner, S. F., & Smeur, E. J. J. (4TU.ResearchData, 2025). Test data of actuator-nonlinear dynamic inversion for systems with heterogeneous actuator dynamics: A superior alternative to incremental nonlinear dynamic inversion [dataset]. [4TU.ResearchData, 2025.] https://doi.org/10.4121/0E146396-715F-43FA-B571-89FEB2906D06

De Ponti, T. M. L., Smeur, E. J. J., & Remes, B. D. W. (2025). Unified-actuator nonlinear dynamic inversion controller for the variable skew quad plane. *Journal of Guidance, Control, and Dynamics*, *48*(5), 1167–1176. https://doi.org/10.2514/1.G008659

De Ponti, T. M. L., Smeur, E. J. J., & Remes, B. W. D. (2023). Incremental nonlinear dynamic inversion controller for a variable skew quad plane. In *2023 International conference on unmanned aircraft systems (ICUAS)* (pp. 241–248). https://doi.org/10.1109/ICUAS57906.2023.10156289

Diane, B., & Remes, W. (2023). Aeronautical vehicle and method of transitioning between flight modes for an aeronautical vehicle. Netherlands Patent Bulletin 46, 15 November 2023.

Li, X., Jiang, Y., Zhang, J., Shi, S., & Zhao, L., et al. (2018). A method to compensate interaction between actuator dynamics and control allocator under incremental nonlinear dynamic inversion controller. *IOP Conference Series: Materials Science and Engineering*, *428*, 012048. https://doi.org/10.1088/1757-899X/428/1/012048

Liu, Y., Steinert, A., Hong, H., Li, H., & Hu, S., et al. (2025). Nonlinear dynamic inversion with generalized actuator dynamics: Performance and stability. *Aerospace Science and Technology*, *162*, 110218. https://doi.org/10.1016/j.ast.2025.110218

Meyer-Brügel, W., & Silvestre, F. J. (2024). Unified control of flight dynamics and actuators using local accelerations. *Journal of Guidance, Control, and Dynamics*, *47*(9), 1920–1938. https://doi.org/10.2514/1.g007860

Oppenheimer, M. W., & Doman, D. B. (2004). Methods for compensating for control allocator and actuator interactions. *Journal of Guidance, Control, and Dynamics*, *27*(5), 922–927. https://doi.org/10.2514/1.7004

Pfeifle, O., & Fichter, W. (2021). Cascaded incremental nonlinear dynamic inversion for three-dimensional spline-tracking with wind compensation. *Journal of Guidance, Control, and Dynamics*, *44*(8), 1559–1571. https://doi.org/10.2514/1.G005785

Raab, S. A., Zhang, J., Bhardwaj, P., & Holzapfel, F., et al. (2018). Proposal of a unified control strategy for vertical take-off and landing transition aircraft configurations. In *Applied aerodynamics conference* AIAA AVIATION Forum. https://doi.org/10.2514/6.2018-3478

Raab, S. A., Zhang, J., Bhardwaj, P., & Holzapfel, F., et al. (2019). Consideration of control effector dynamics and saturations in an extended INDI approach. In *AIAA Aviation 2019 forum*. https://doi.org/10.2514/6.2019-3267

Sieberling, S., Chu, Q. P., & Mulder, J. A., et al. (2010). Robust flight control using incremental nonlinear dynamic inversion and angular acceleration prediction. *Journal of Guidance, Control, and Dynamics*, *33*(6), 1732–1742. https://doi.org/10.2514/1.49978

Simplício, P., Pavel, M. D., van Kampen, E., & Chu, Q. P., et al. (2013). An acceleration measurements-based approach for helicopter nonlinear flight control using incremental nonlinear dynamic inversion. *Control Engineering Practice*, *21*(8), 1065–1077. https://doi.org/10.1016/j.conengprac.2013.03.009

Smeur, E. J. J., Chu, Q., & de Croon, G. C. H. E., et al. (2016a). Adaptive incremental nonlinear dynamic inversion for attitude control of micro air vehicles. *Journal of Guidance, Control, and Dynamics*, *39*(3), 450–461. https://doi.org/10.2514/1.G001490

Smeur, E. J. J., de Croon, G. C. H. E., & Chu, Q., et al. (2018). Cascaded incremental nonlinear dynamic inversion for MAV disturbance rejection. *Control Engineering Practice*, *73*, 79–90. https://doi.org/10.1016/j.conengprac.2018.01.003

Smeur, E. J. J., De Croon, G. C. H. E., & Chu, Q., et al. (2016b). Gust disturbance alleviation with incremental nonlinear dynamic inversion. In *IEEE/RSJ International conference on intelligent robots and systems* (pp. 5626–5631). https://doi.org/10.1109/IROS.2016.7759827

Smeur, E. J. J., Hoppener, D. C., & Wagter, C. D. (2017). Prioritized control allocation for quadrotors subject to saturation. *International Micro Air Vehicle Conference and Flight Competition*. https://www.imavs.org/papers/2017/6.pdf.

Steffensen, R., Ginnell, K., & Holzapfel, F., et al. (2024). Practical system identification and incremental control design for a subscale fixed-wing aircraft. *Actuators*, *13*(4), 130. https://doi.org/10.3390/act13040130

Steffensen, R., Steinert, A., & Smeur, E. J. J. (2023). Nonlinear dynamic inversion with actuator dynamics: An incremental control perspective. *Journal of Guidance, Control, and Dynamics*, *46*(4), 709–717. https://doi.org/10.2514/1.G007079

Steinert, A., Raab, S., Hafner, S., Holzapfel, F., & Hong, H., et al. (2025). From fundamentals to applications of incremental nonlinear dynamic inversion: A survey on INDI – part I. *Chinese Journal of Aeronautics*. https://doi.org/10.1016/j.cja.2025.103553

Wang, X., Van Kampen, E., Chu, Q. P., & De Breuker, R. (2019). Flexible aircraft gust load alleviation with incremental nonlinear dynamic inversion. *Journal of Guidance, Control, and Dynamics*, *42*(7). https://doi.org/10.2514/1.g003980

Zhou, Y., Ho, H. W., & Chu, Q. (2021). Extended incremental nonlinear dynamic inversion for optical flow control of micro air vehicles. *Aerospace Science and Technology*, *116*, 106889. https://doi.org/10.1016/j.ast.2021.106889